Journal of Nanobiotechnology

RESEARCH

Open Access

AI-assisted SERS imaging method for label-free and rapid discrimination of clinical lymphoma

Haiting Cao[2†], Xiaofeng Wu[1†], Huayi Shi[2†], Binbin Chu[2*], Yao He[2,3,4*], Houyu Wang[2*] and Fenglin Dong[1*]

Abstract

Background Lymphoma is a malignant tumor of the immune system and its incidence is increasing year after year, causing a major threat to people's health. Conventional diagnosis of lymphoma basically depends on histological images consuming long-time and tedious manipulations (e.g., 7–15 days) and large-field view (e.g., > 1000 × 1000 μm^2). Artificial intelligence has recently revolutionized cancer diagnosis by training pathological image databases via deep learning. Current approaches, however, remain dependent on analyzing wide-field pathological images to detect distinct nuclear, cytologic, and histomorphologic traits for diagnostic categorization, limiting their applicability to minimally invasive lesion.

Results Herein, we develop a molecular imaging strategy for minimally invasive lymphoma diagnosis. By spreading lymphoma tissue sections tightly on a surface-enhanced Raman scattering (SERS) chip, label-free images of DNA double strand breaks (DSBs) in 30 × 30 μm^2 tissue sections could be achieved in ~ 15 min. To establish a proof of concept, the Raman image datasets collected from clinical samples of normal lymphatic tissues and non-Hodgkin's lymphoma (NHL) tissues were well organized and trained in a deep convolutional neural network model, finally achieving a recognition rate of ~ 91.7 ± 2.1%.

Conclusions The molecular imaging strategy for minimally invasive lymphoma diagnosis that can achieve a recognition rate of ~ 91.7 ± 2.1%. We anticipate that these results will catalyze the development of a series of histological SERS-AI technologies for diagnosing various diseases, including other types of cancer. In this work, we present a reliable tool to facilitate clinicians in the diagnosis of lymphoma.

Keywords SERS, Convolutional neural network, Lymphoma, Minimally invasive diagnosis

†Haiting Cao, Xiaofeng Wu, and Huayi Shi have contributed equally to this work.

*Correspondence:
Binbin Chu
bbchu@suda.edu.cn
Yao He
yaohe@suda.edu.cn
Houyu Wang
houyuwang@suda.edu.cn
Fenglin Dong
fldong@suda.edu.cn
Full list of author information is available at the end of the article

Graphical Abstract

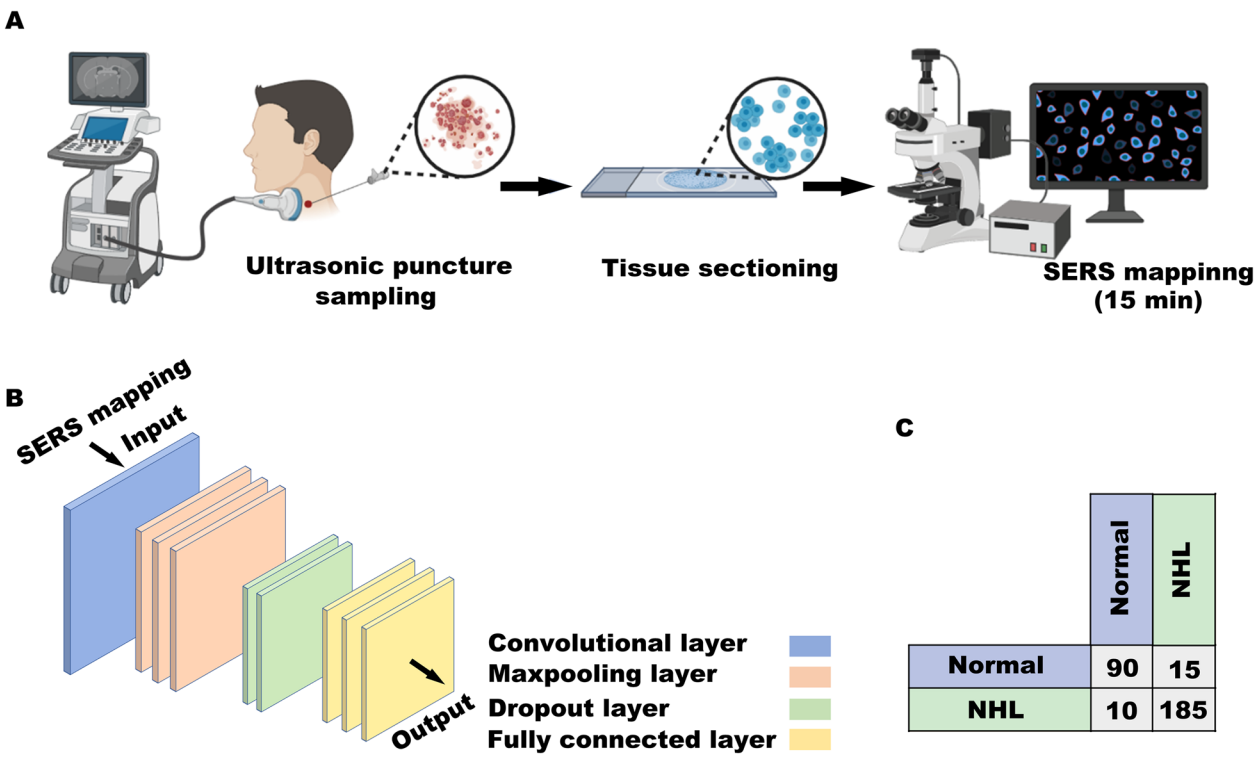

Introduction

Currently, the clinical technique for the diagnosis and classification of lymphoma is ultrasound-guided core needle biopsy (UGCNB) assisted with histopathological analysis [1–5]. UGCNB can accurately and minimally obtain lesion tissues, improving the sampling rate and thus avoiding misdiagnosis caused by unqualified sampling. It is worth pointing out that, the subsequent histopathological analysis has relatively complicated experimental procedures, including frozen sectioning and cytological preparations, consuming a long diagnosis circle (e.g., 7–15 days) [6–9]. Moreover, the identification of microscopic architectural features requires a large-field view (e.g., > 1000×1000 μm^2) of histological images. In addition, the pathological results should be interpreted by skilled technicians or clinicians, which places great burdens on developing countries, wherein medical human resources are relatively scarce [10].

On the other hand, artificial intelligence (AI) has recently revolutionized cancer diagnosis by training the database of pathological images through neural networks [11–28]. Recently, the stimulated Raman scattering (SRS) technique has been employed to simulate hematoxylin–eosin (H&E) staining in a label-free manner, followed by the convolutional neural network (CNN) training and testing [29, 30]. However, these SRS-based methods still adhere to the histopathological interpretation principle to identify histomorphologic, cytologic and nuclear features. The features should be extracted from slide images with a large image scale, restricting the applications to minimally invasive lesions. Distinguished from SRS, which reveals the spectroscopic information of C-H bonds, SERS inherits the rich chemical fingerprint spectroscopic information and amplifies Raman signals by several orders of magnitude by plasmon-enhanced scattering and excitation [31–41].

Making use of unique merits of AI and SERS, we herein present an AI-assisted SERS (AI-SERS) strategy for the minimally invasive diagnosis of clinic lymphoma sample in a swift and label-free manner. Of particular significance, a SERS mapping image of lymphoma tissues with an area of 30×30 μm^2 can be achieved within 15 min through attaching the lymphoma slice sample onto the surface of a SERS chip, the silicon wafer functionalized with silver nanoparticles (Ag NPs@Si) via surface modification (Fig. 1a). In our case, we collected

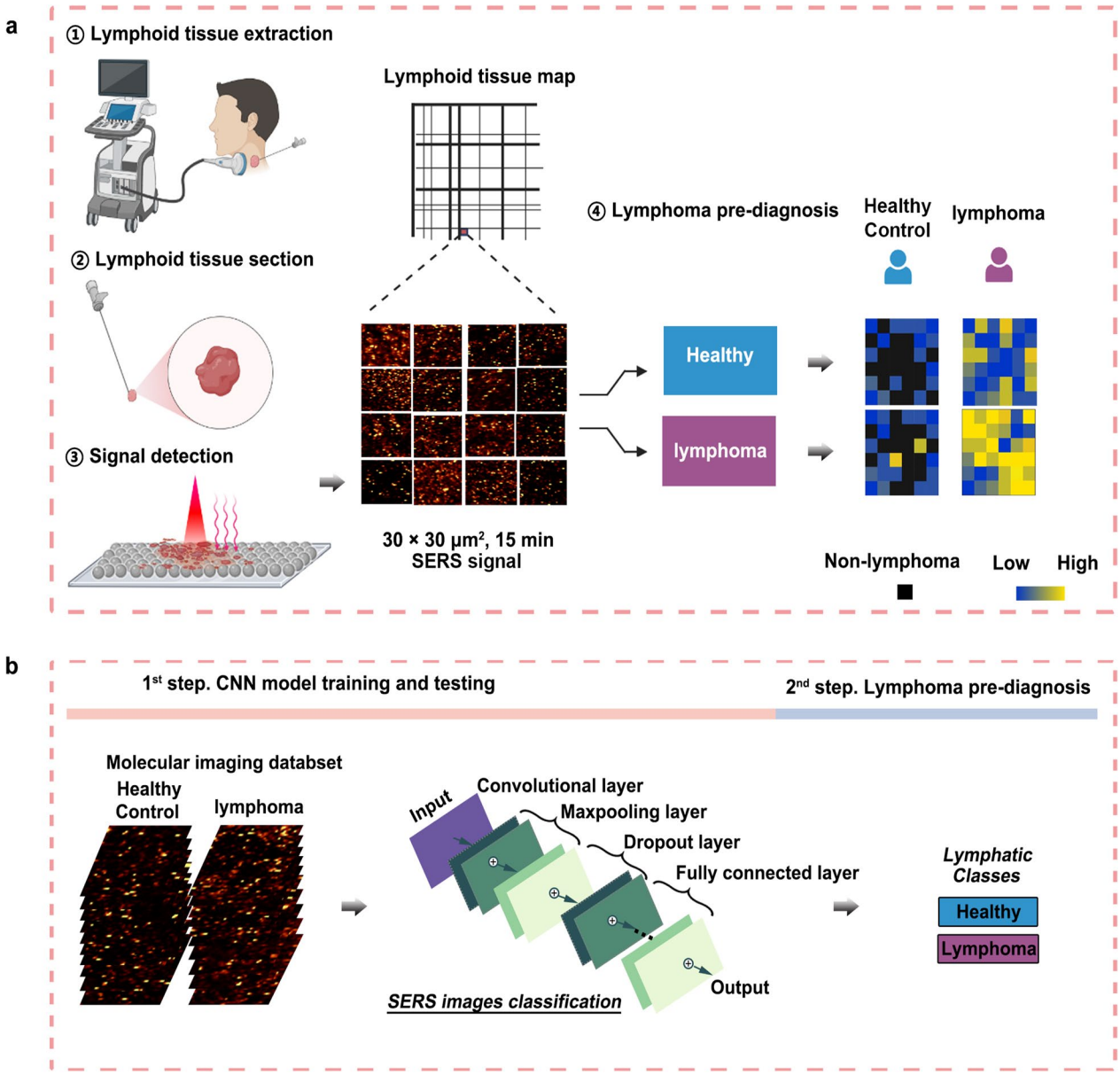

Fig. 1 Schematic illustration of SERS imaging of clinical lymphatic sections for the diagnosis of lymphoma assisted by a silicon-based SERS chip coupled with deep learning. **a** Overview. When the lymphoma slice sample received from ultrasound-guided core needle biopsy (UGCNB) is attached to the surface of the SERS chip, two-dimensional SERS scanning of lymphoma tissue with an area of 30 × 30 μm^2 can be completed in less than 15 min. SERS signals (40 × 40 points) were detected from per sample and analysed by a convolutional neural network (CNN). The system outputs predict the presence of lymphoma. The heat map displays representative examples of predicted outcomes for lymphoma status. **b** The process of the CNN framework. The CNN model includes a convolutional layer, a max-pooling layer, a dropout layer and a fully connected layer. In the first step, the two-dimensional SERS imaging was input to the CNN model to optimise the performance of the CNN. Subsequently, the type of lymphoma samples was performed to identify

900 two-dimensional SERS mapping points from clinical samples, including normal lymphoma and non-Hodgkin's lymphoma (NHL) from healthy donors as well as lymphoma patients (Fig. 1b). After training in the CNN model, the resultant SERS images of normal lymphoma and non-Hodgkin's lymphoma can be precisely distinguished with an accuracy rate as high as ~ 91.7 ± 2.1%.

Materials and methods

Preparation of silicon SERS chip

Hydrofluoric acid-assisted galvanic deposition was used to create silicon SERS substrates made of Ag NPs that had been uniformly modified on a silicon wafer. To fabricate silver nanoparticle-decorated silicon substrates (Ag NPs@Si) for SERS applications, a rectangular silicon specimen (4.0 cm × 4.0 cm) underwent sequential chemical treatments. Initially, the native silicon dioxide layer was etched through immersion in 5% hydrofluoric acid solution for 30 min. Subsequent metallization was achieved by exposing the activated silicon surface to an aqueous mixture containing 1.25 mM silver nitrate in 10% HF, facilitating spontaneous silver nanoparticle deposition through galvanic displacement. The synthesized hybrid material underwent post-processing to enhance stability, including triple-rinsing with deionized water to eliminate residual reactants and prevent surface oxidation, followed by dehydration using a gentle nitrogen stream. This optimized protocol ensures reproducible formation of oxidation-resistant Ag NPs@Si surfaces suitable for spectroscopic applications.

Clinical tissue samples obtained by UGCNB

Clinical tissue samples (Table S1) without any identifying information were collected at the First Affiliated Hospital of Soochow University (Suzhou, China) with informed consent. The Ethics Committee of First Affiliated Hospital of Soochow University approved this study (Audit Number: (2023) LUN Research Batch No. 314 approvals for healthy control and NHL, respectively). In detail, the patient showed a proper position (supine or lateral position) to fully expose the corresponding lesions of the lymph node (e.g., neck, axilla, etc.). The ultrasonic diagnostic equipment of GE LOGIQ E9 (2–9 MHz, 9–15 MHz) and MyLabTwice (3–11 MHz, 4–13 MHz) equipped with ARGON biopsy needles (SuperCore Biopsy Instrument, MCXS1609LX) were employed to determine the locations of lesions and minimally obtain the corresponding tissue samples. Typically, the ML6-15 or LA523 linear array probe was employed to perform two-dimensional multi-section ultrasound scanning to determine the location and size of the lymph node, internal echo, blood flow, and adjacent relationship with surrounding tissues. Afterwards, 1.0 or 2.4 mL of contrast agent was diluted with 5 ml of saline, and then 5 ml of saline was injected through the median cubital vein in sequence. Meanwhile, the 9 L or LA332 probe was employed to perform ultrasound imaging. During ultrasound imaging, the perfusion of lymph nodes and surrounding tissues was monitored in real time to mark the puncture points on the body surface and design the optimal puncture path, avoiding the regions without enhancement and surrounding large blood vessels, nerves and important organs. The skin, probes, and drapes were routinely sterilized, and 2% lidocaine was used for local infiltration anaesthesia. During the puncture process, ultrasound imaging was used to monitor and adjust the needle direction in real time. After confirming the best puncture path, the trigger of the biopsy needle was pressed to obtain a tissue strip. According to the clinical requirements, tissue strips could be taken multiple times by repeating the above operation procedures. The obtained tissue strips were immediately fixed in a 10% formalin solution or placed at −80 °C for the following experiments. During the surgical process, the vital signs of patients should be carefully evaluated. After the surgery, the patient can leave or return to the ward without discomfort. This study employed retrospectively obtained samples as this study aims to create a technology that might be used by clinicians to identify normal and lymphoma patients, the time period for enrollment and data collection was not identified.

SERS imaging

Two-dimensional SERS imaging was performed by integrating the area of the peak with the Raman shift at 1588 cm^{-1}. In addition, to investigate the assignments of the Raman shift at 1588 cm^{-1}, DNA samples were irradiated with UV or treated with hydrogen peroxide, followed by SERS measurements. In the UV induction experiment, the genomic DNA of RPMI cells was first extracted with the kit, and then the extracted DNA samples were irradiated with a UV lamp for 0, 0.5, and 2 h. Finally, the samples were tested with a confocal Raman spectrometer. In the hydrogen peroxide induction experiment, the RPMI cells were first cultured in a medium containing 0, 0.1, and 1 mM hydrogen peroxide for 6 h, and then the genomic DNA of each group of cells was extracted using the kit. Finally, the extracted genomic DNA samples were tested using a confocal Raman spectrometer. Raman spectra were obtained using a WITec alpha300 R equipped with a Ne-He laser (532 nm, 0.8 mW) and a Zeiss EC Epiplan 50x. Each sample of the section attached to Ag NPs@Si was independently scanned at 20 different positions, with the scanning area of 30 μm × 30 μm. The detailed parameters for Raman measurements were as follows: excitation wavelength of 532 nm, the laser power of 0.8 mW, integration time of 0.5 s, scanning step of 40 × 40, and collection interval of 0–3600 cm^{-1}. The obtained Raman spectra and Raman mapping were further analysed and exported by WITec Project FIVE 5.1 software.

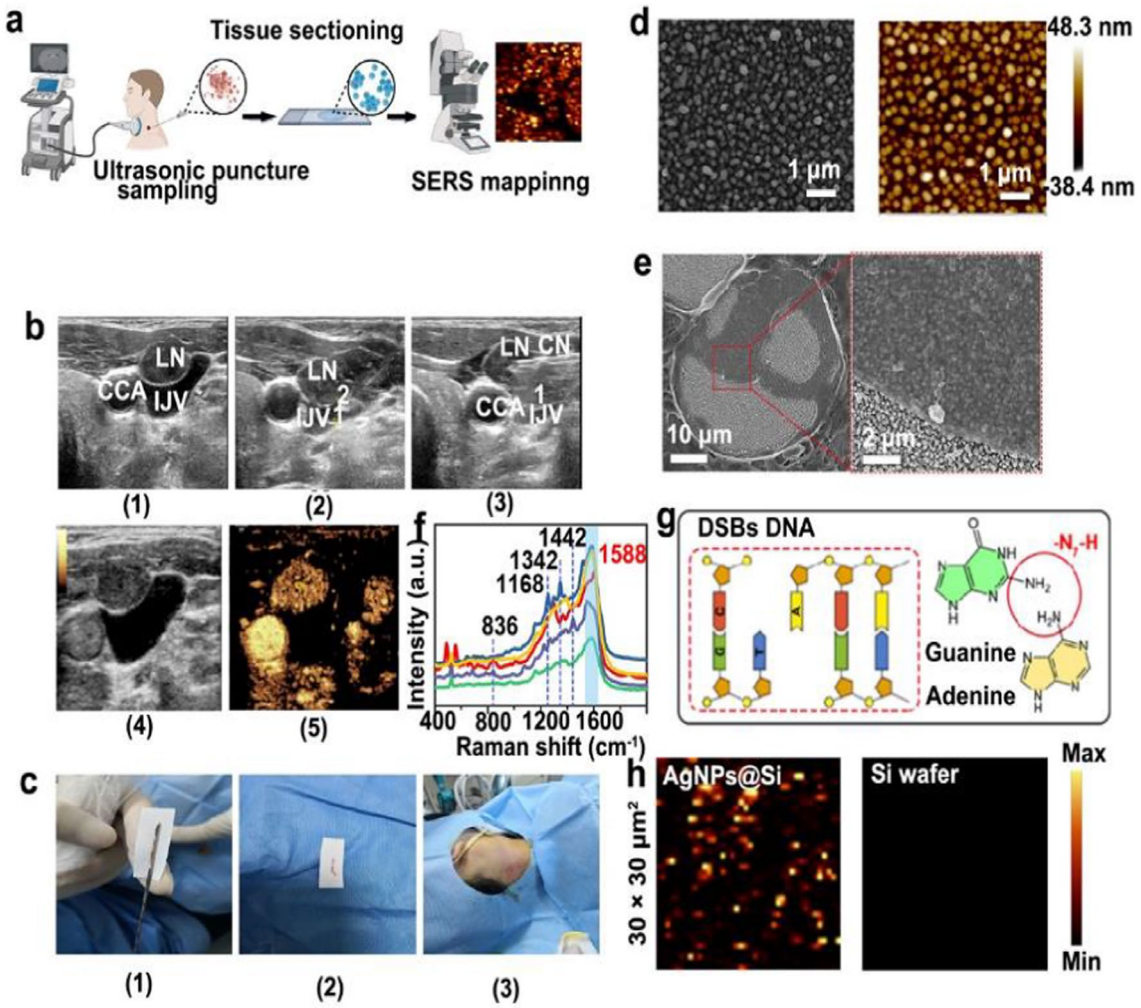

Fig. 2 Collection of clinical lymphatic sections by ultrasound-guided core needle biopsy (UGCNB) followed by SERS measurements via a silicon-based SERS chip. **a** A scheme illustrating the collection of lymphatic sections by UGCNB followed by SERS measurements via a silicon-based SERS chip. **b** Precise collection of lymphatic tissues by UGCNB and corresponding. **c** Surgical operations. *LN* lymph node, *CCA* common carotid artery, *IJV* internal jugular vein, *CN* thick needle. **b-(1)** An abnormal lymph node is observed in the IV area of the right cervical close to the common carotid artery and internal jugular vein (the size is approximately 18 mm × 8 mm), wherein the lymphatic hilum echo disappears. **b-(4,5)** The abnormal lymph node is uniformly enhanced; no necrosis is observed. **b-(2)** Use an anaesthetic needle to inject normal saline between the internal jugular vein and the lymph nodes to form a safety isolation zone. **b-(3)** A 16G semiautomatic biopsy needle is punctured into the right cervical area IV lymph node inside, triggering ejection and withdrawing the needle. Under the premise of ensuring safety, obtain the number of tissue strips as needed. **c-(1), (2)** Tissue strips taken out by the 16G semiautomatic biopsy needle. **c-(3)** Only punctate wounds remain on the patient's neck puncture site, followed by pasting with an applicator. **d** SEM and AFM images of Ag NPs@Si. **e** SEM images of lymphatic sections attached to Ag NPs@Si. **f** Typical Raman spectra collected from lymphoma sections attached to Ag NPs@Si. **g** Schematic illustration of the exposure of $-N_7$-H in guanine and adenine caused by DNA double-strand breaks (DSBs). **h** SERS mapping at 1588 cm^{-1} collected from sections on Ag NPs@Si and silicon wafer. Excitation wavelength = 532 nm, laser power = 0.8 mW, acquisition time = 1 s. All imaging experiments were repeated three times with similar experimental conditions and results

The architecture of the CNN and training

The architecture of CNN includes four layers: a convolutional layer (filters = 4, kernel size of 6 × 6), a max pooling layer (pool size of 2 × 2), a dropout layer (dropout rate = 0.2) and a fully connected layer. The original molecular images were transferred by four convolution kernels in the convolutional layer, followed by size reduction in the max pooling layer and pixel dropping in the dropout layer. The nonlinear activation functions of ReLU and softmax were subsequently employed to fit the data with outputs in the fully connected layer. The workflow prioritizes identifying lymphoma samples through prediction, then directly categorizes them into normal or NHL lymphoma types. For CNN model development, the

molecular imaging dataset was split into a training subset (810 images) and a test subset (90 images). Network architecture design, data preprocessing, and training procedures were executed using TensorFlow (version 2.1), an open-source machine learning framework developed by Google (Table S2).

Results and discussion

UGCNB-guided SERS detection of lymphoma sections

The lymphoma tissue strips were initially minimally obtained using the UGCNB method, followed by label-free SERS mapping (Fig. 2a). Two-dimensional ultrasound multislice scanning was utilized to assess the fundamental health of suspicious lymph nodes. As shown in Fig. 2b, we recorded and observed the perfusion of the lymph nodes and the adjacent relationship with peripheral blood vessels, nerves and other important structures in real time under the ultrasound contrast mode. Afterwards, we designed the puncture path and labelled the puncture point on the body. To harvest the tissue strips, we then performed routine preoperative preparations by using a disposable biopsy needle (16 G × 9 cm) for target lymph node puncture (Fig. 2c). Lymphatic sections with a thickness of 2 μm were cut and spread on Ag NPs@Si or glass slides. Notably, lymphoid sections attached to glass slides underwent routine histological manipulations, including dewaxing, hydration and staining, while sister lymphoid sections on Ag NPs@Si underwent the same processing except for staining (Fig. S1). We synthesized Ag NPs@Si by using the silicon-based galvanic deposition method, as previously reported [42–45]. The in situ growth of uniform silver nanoparticles on silicon substrates occurs through redox reactions mediated by surface Si–H bonds formed during HF treatment. When silver nitrate solution interacts with hydrofluuoric acid-etched silicon wafers, Ag^+ ions undergo reduction at the semiconductor interface, resulting in the direct formation of metallic silver nanostructures. Atomic force microscopy (AFM) and scanning electron microscopy (SEM) characterization confirms the homogeneous distribution of spherical Ag nanoparticles with an average size of 180 nm across the silicon surface. This self-limiting deposition process effectively stabilizes the nanoparticles without requiring external stabilizing agents, as the activated Si–H terminated surface simultaneously provides both reducing electrons and anchoring sites for metallic silver nucleation (Fig. 2d). As a result, the Ag NPs@Si featured a good SERS reproducibility. As shown in the SERS mapping spectra of 10^{-4} M R6G in Fig. S2, the relative standard deviation (RSD) value of the SERS intensity of R6G at 1364 cm^{-1} is 4.33%. In addition to adaptable reproducibility, the Ag NPs@Si also featured distinct SERS effects. As simulated by finite-difference-time-domain (FDTD) (Fig. S3), we observed relatively strong electromagnetic (EM) fields around Ag NPs and in the gap between Ag NPs and the silicon surface in Ag NPs@Si. The corresponding SERS enhancement factor (EF) of Ag NPs@Si was calculated to be 1.5×10^6 (the detailed EF calculation can be found in the Note S1).

To focus on examining the SERS signal source of lymphoma sections, we used SEM and confocal Raman microscopy to characterize lymphoma section samples attached to AgNPs@Si substrates. As illustration in Fig. 2e, the SEM image showed that the section sample and AgNPs were in close contact, which was critical for generating increased Raman signals of biological components within plasmonic gaps. To avoid burning damage during laser irradiation, we rigorously investigated the laser power and finally set it at 0.8 mW to obtain stable intrinsic Raman spectra. As revealed in Fig. 2f, we detected subtle Raman peak and intensity variations in several regions near 836, 1168, 1342 and 1558 cm^{-1}, which were assigned to the H-bonding of the indole ring in tyrosine, the ring stretch in guanine, the N–H/C-H band in amide III/a-helix and N_7-H in guanine/adenine, respectively (Table S3). In our initial attempt, we focused on SERS mapping the 1588 cm^{-1} peaks that were the clearest Raman peak. Previous studies have shown that

(See figure on next page.)

Fig. 3 Detection of DNA double-strand breaks by SERS. **a** SERS spectra of genomic DNA extracted from RPMI cells with UV radiation or not. **b** SERS mapping of genomic DNA extracted from HUT78 cells at 1588 cm^{-1} with and without hydrogen peroxide (H_2O_2) treatment. **c** H&E images and bright-field images in Raman mode collected from diffuse large B lymphoma. Clinical paraffin-embedded diffuse large B lymphoma tissue was sliced into multiple parts, followed by H&E staining and SERS mapping. Three zoomed-in sections (the region of damage (red frame), the boundary of cell inflammation (blue frame) and nonpathological regions (green frame) selected from one sister section's H&E images are colocalized in the matching bright-field images in Raman mode of another sister section. Afterwards, the three selected regions are subjected to SERS mapping. **d** The overlapping of SERS mapping of DNA DSBs at 1588 cm^{-1} with immunostaining of DNA DSB markers by using anti-H2A.X. **e** H&E image, CD20, CD79a immunostaining image and bright-field image in Raman mode collected from consequent sections of NK/T lymphoma sample. **f** H&E images and bright-field images in Raman mode collected from consequent sections of MALT, follicular, NK/T and peripheral T lymphoma. Positions of zoom-in frames in bright-field images were chosen to perform SERS mapping according to pathological features. **g** The SERS mapping of healthy control and NHL lymphoma. Excitation wavelength = 532 nm, laser power = 0.8 mW, acquisition time = 1 s. All imaging experiments were repeated three times with similar experimental conditions and results

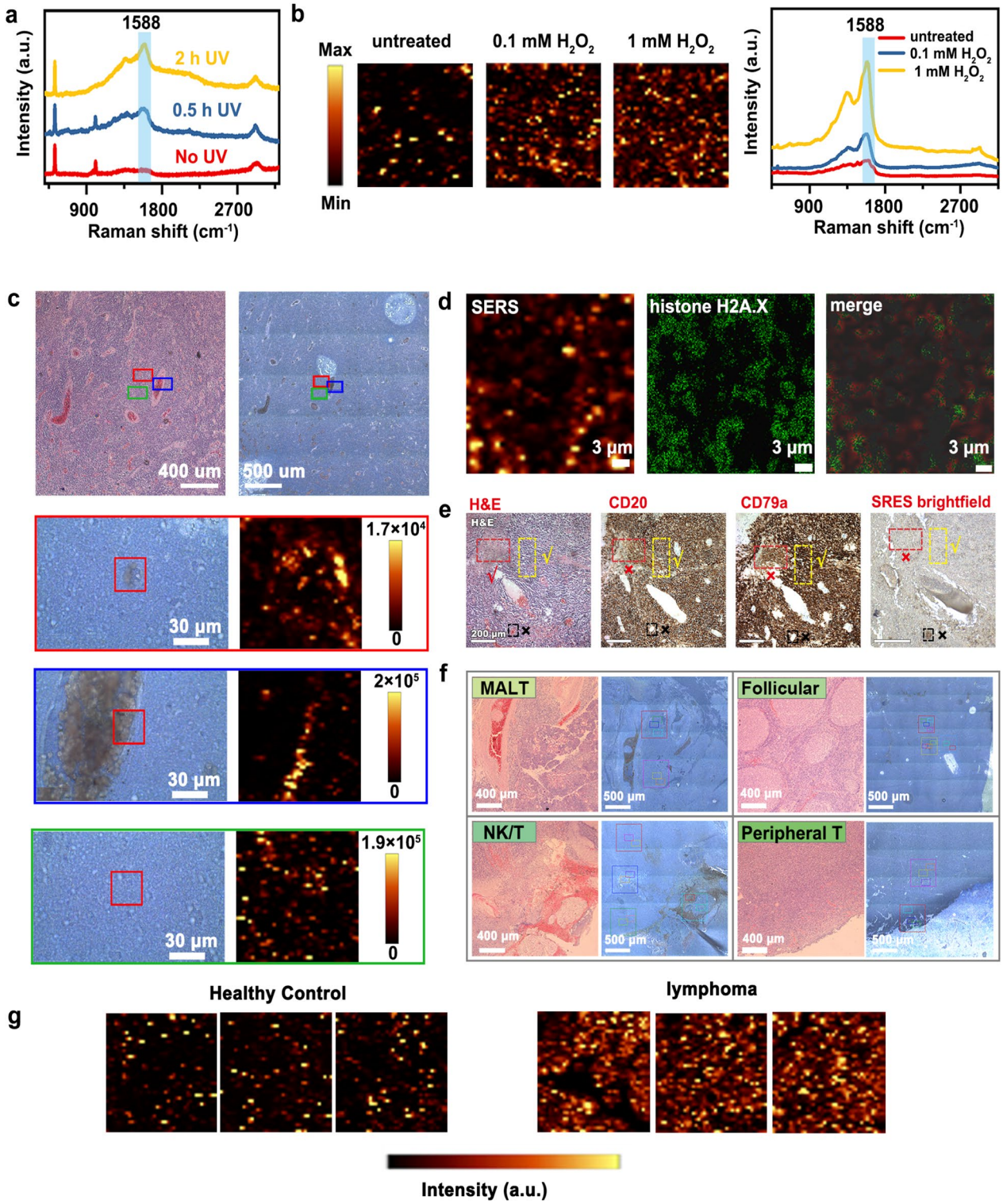

Fig. 3 (See legend on previous page.)

the enhanced Raman signals at 1588 cm^{-1} were caused by DNA double-strand breaks (DSBs), which exposed N_7-H in guanine and adenine (Fig. 2g) [46–48]. Therefore, by evaluating the SERS signal intensity at 1588 cm^{-1}, it may be possible to perform label-free imaging of DNA DSBs in lymphoma slice samples. To further clarify the

significant role of silicon-based SERS substrates, we compared the SERS enhancement of the lymphoma section samples to Ag NPs@Si substrates and pure silicon wafers under the same conditions. As shown in Fig. 2h, distinct SERS mapping signals at 1588 cm^{-1} of lymphoma slices were observed only on the constructed Ag NPs@Si substrate rather than the silicon wafer, demonstrating that Ag NPs@Si substrate can effectively increase the intrinsic Raman signal intensity of lymphoma slice samples.

Detection of DNA double-strand breaks by SERS

As the typical form of DNA fragmentation, DNA DSBs can be induced by UV irradiation and hydrogen peroxide treatment and are also present in many cellular events, such as apoptosis and inflammation [49–53].To demonstrate whether the change in the SERS signal at 1588 cm^{-1} obtained from lymphatic sections was associated with DNA DSBs, we first extracted genomic DNA from RPMI cells and then treated them with or without UV irradiation (e.g., 0, 0.5, or 2 h), followed by SERS detection. As expected, after 2 h of UV irradiation, the extracted DNA showed the highest SERS spectral intensity at 1588 cm^{-1} (Fig. 3a). Next, we investigated whether DNA DSBs in healthy doners would cause changes in SERS signaling at 1588 cm^{-1}. Experimentally, HUT78 cells were treated with or without H_2O_2 (e.g., 0, 100 μM, or 1 mM) for 4 h to induce different levels of intracellular DNA DSBs. Indeed, the Raman intensity at 1588 cm^{-1} became progressively sharper when treated with higher concentrations of H_2O_2. As a result, the SERS profiles of the 1 mM H_2O_2-treated group showed more bright spots compared to the untreated and 100 μM H_2O_2-treated groups (Fig. 3b). These results indicated that the SERS spectra of genomic DNA samples treated with UV or hydrogen peroxide showed higher SERS signal intensity at 1588 cm^{-1}.

To demonstrate that the SERS image could overlap with the clinical histological images, clinical paraffin-embedded tissue of diffuse large B lymphoma was cut into several consequent sections. Specifically, the two sister sections were subjected to H&E staining and SERS mapping. As shown in Fig. 3c, three magnified regions (i.e., red, blue, and green frames) selected from the H&E image view of one sister slice were colocalized in the corresponding bright-field image in Raman mode of the other sister slice. Afterwards, the three chosen regions were subjected to SERS mapping. Typically, the region of damage (red frame), the boundary of cell inflammation (blue frame) and nonpathological regions (green frame) were clearly revealed by distinct SERS mapping signals. Ultimately, we used anti-H2AX (a phosphorylated histone antibody) to visualize DNA DSBs by immunostaining. As shown in Fig. 3d, the SERS signal at 1588 cm^{-1} overlapped well with the immunofluorescence signal of H2AX, indicating that the SERS signal at 1588 cm^{-1} originated from the DSB of DNA. These results revealed that Ag NPs@Si enabled label-free detection of DNA DSBs in lymphoma sections.

The proposed strategy was based on SERS mapping with a size of 30 × 30 $μm^2$. At such a size, it was necessary

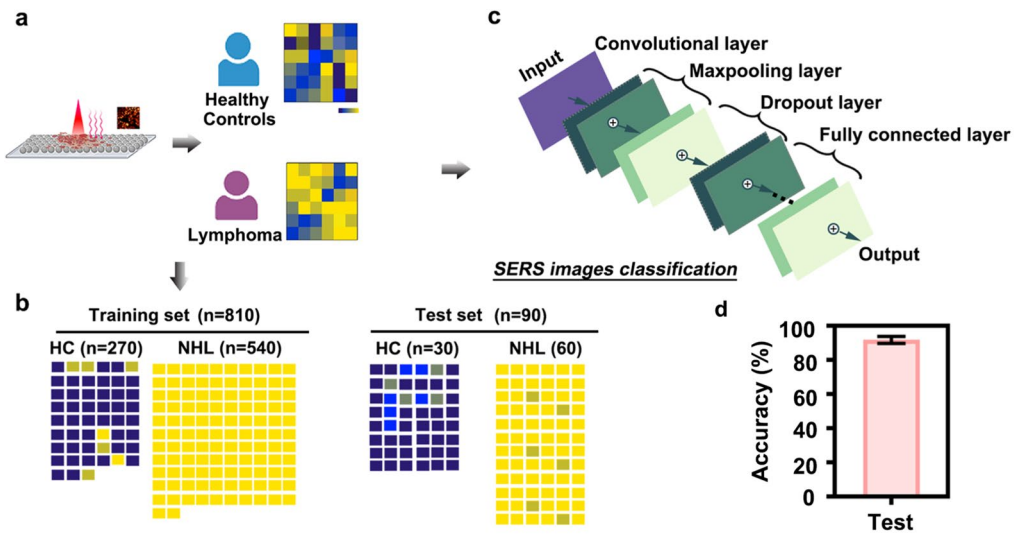

Fig. 4 SERS-AI platform for the diagnosis of lymphoma by combining SERS mapping and CNN. **a** The General schematic of the CNN model for recognition. The collected SERS imaging will be identified as healthy or NHL lymphoma. **b** Training of the CNN classifier. Healthy and lymphoma patient samples were randomly split into training (n = 810) and testing (n = 90) sets. All data were comprehensively labeled by sample type. **c** The structure of a CNN model. **d** The average accuracy for two lymphatic classes. Statistical analysis was performed using one-way ANOVA

to accurately localize cancerous regions in heterogeneous lymphoma tissues. Therefore, we performed H&E staining, immunohistochemistry and bright-field colocalization in Raman mode on the collected lymphoma sections. As shown in Fig. 3e, vascular and extracellular matrix regions could be easily excluded from the H&E images and immune histochemical images of diffuse large B lymphoma samples (black frames) for SERS mapping. Regions with single-negative or double-negative CD20 and CD79a staining results were also excluded (red frames), whereas only regions with double-positive staining results were selected for SERS mapping by colocalization with the bright-face maps (yellow frames) in Raman mode. SERS profiles of normal lymphoid samples in the training dataset were collected from random areas of normal slices. In addition, we created a test dataset containing 90 SERS imaging data points of randomly acquired solid regions, including cancerous, noncancerous, and heterogeneous regions, from H&E images of mucosa-associated lymphoid tissues (MALT), follicular lymphomas, NK/T lymphomas, and peripheral T lymphomas (Fig. 3f). This data acquisition method was closer to the actual diagnosis. After data acquisition, we found that the typical molecular images of normal lymphoid tissues and NHL showed different densities of DNA DSB distribution. Among them, NHL had the higher density of DSBs, while normal tissues had the lower density of DSBs (Fig. 3g, and Figs. S4 & S5).

SERS-AI platform for diagnosis of lymphoma by combining SERS mapping and CNN

For the discrimination of cancerous and noncancerous clinical lymphoma samples in the CNN model, a dataset containing 900 SERS imaging data was first collected by setting a standardized SERS mapping process. Then, in order to avoid the classifier being familiar with the data in the test set [54], 810 images of the above-obtained molecular imaging dataset was randomly separated into training set for CNN training, and another 90 images was randomly separated into test set for validation (Fig. 4a, b). After data collection, we built a deep convolutional neural network containing convolutional layer, maxpooling layer, dropout layer and fully connected layer (Fig. 4c). Images in molecular imaging dataset were reshaped with a resolution of 119×119 and convoluted by a filter of 5×5. After the training and testing of the CNN model in the training subset and the test subset, the CNN model performance reaches excellent performance.

Of the 100 healthy samples, 90 were identified as healthy and 10 as NHL. 185 of the 200 NHL samples were identified as NHL, and 15 of the 200 NHL samples were identified as healthy. All three hundred healthy and NHL samples were identified as healthy and NHL with an identification rate of ~ 91.7%. Significantly, we further iterated the process of differentiating the test set data using the CNN for three times [55]. In detail, the accuracy on each of the three times was ~ 90%, ~ 91% and ~ 94%, the average accuracy was calculated as $\sim 91.7 \pm 2.1\%$. (Fig. 4d) [53–55]. Receiver operating characteristic (ROC) curves were further utilized to assess the performance (Figs. S6 & S7). The areas under the ROC curves of the three lymphatic classes were 0.90 for HC, 0.92 for NHL, demonstrating an acceptable accuracy for lymphoma classification from lesions or minimally invasive lesions. In addition, we optimized the optimal number of epochs for CNNs and came up with an optimal epoch of 10 (Fig. S8) [53–55].

Conclusion

In summary, a novel AI-SERS strategy is developed for the rapid and minimally invasive diagnosis of lymphoma, in which UGCNB is used for sampling, SERS chip is employed for imaging of lymphoma samples and CNN is exploited for AI recognition. Of particular significance, two-dimensional SERS mapping of lymphoma tissues with an area of 900 μm^2 could be achieved within 15 min, on the basis of which, clinic samples of healthy control and NHL are readily discriminated assisted by deep learning, with a high accuracy rate of up to $\sim 91.7 \pm 2.1\%$. These results open exciting opportunities for developing novel AI-based strategies for myriad biochemical analysis and detection, especially for rapid and noninvasive diagnosis of malignant tumors.

Supplementary Information

The online version contains supplementary material available at https://doi.org/10.1186/s12951-025-03339-5.

Supplementary material 1: Note S1. Comparison of the enhancement effect of silicon wafers modified with silver nanoparticleswith that of pure silicon wafers. Table S1. Clinical information of clinical tissue samples without any identifying information. Table S2. The information on implementing the deep learning. Table S3. Gender and average age of HC and NHL tissue sections providers. Figure S1. Preparation of lymphatic sections attached onto SERS substrates. Figure S2. The size distribution of AgNPs@Si. Figure S3. The electromagnetic field intensitydistribution of Ag NPs@Si by the FDTD simulation. Figure S4. SERS imaging dataset of normal lymphatic samples. Figure S5. SERS imaging dataset of B-cell non-Hodgkin's lymphomasamples. Figure S6. ROC curves of healthy control. Figure S7. ROC curves ofsamples. Figure S8. The average accuracy for two lymphatic classes by the CNN.

Acknowledgements
We appreciate the financial support from Program for Jiangsu Specially Appointed Professors to Prof. Yao He, a project funded by the Priority Academic Program Development of Jiangsu Higher Education Institutions (PAPD), 111 Project as well as the Collaborative Innovation Center of Suzhou Nano Science and Technology (NANO-CIC).

Author contributions
HTC, HYS, BBC, HYW, YH and FLD conceived the idea, discussed the data and prepared the manuscript. HYS and HTC performed the design, construction and characterization of CNN system. XFW performed the biological experiments and analyzed the data.

Funding
Fenglin Dong for the research described in this study from Special Project for Clinical Key Diseases in Diagnosis and Treatment Technology of Suzhou (LCZX202104), the Talent Research Project for Health Talent Plan of Gusu (GSWS2023008), and the Doctoral Clinical Research Project at First Affiliated Hospital of Soochow University (BXLC002). *Yao He* discloses support for the research described in this study from the National Natural Science Foundation of China (Nos. 22393932 and T2321005), the National Key R&D Program of China (No. 2023YFB3208200), the Science and Technology Development Fund, Macau SAR (Nos. 0002/2022/AKP, and 0115/2023/RIA2). *Houyu Wang* provided support for the research described in this study from the National Natural Science Foundation of China (No. 22074101). *Binbin Chu* provided support for the research described in this study from the National Natural Science Foundation of China (No. 22204117 and 22474084).

Availability of data and materials
No datasets were generated or analysed during the current study.

Declarations

Ethics approval and consent to participate
The non-interventional research protocols of clinical pathological samples (including normal lymphoma and non-Hodgkin's lymphoma (NHL) from healthy donors and lymphoma patients) used in the present study were approved by the Ethics Committee of the First Affiliated Hospital of Soochow University [Audit Number: (2023) LUN Research Batch No. 314 approvals].

Consent for publication
Not applicable.

Competing interests
The authors declare no competing interests.

Author details
[1]Department of Ultrasound, The First Affiliated Hospital of Soochow University, Suzhou 215031, Jiangsu, China. [2]Suzhou Key Laboratory of Nanotechnology and Biomedicine, Institute of Functional Nano & Soft Materials (FUNSOM), and Collaborative Innovation Center of Suzhou Nano Science and Technology (NANO-CIC), Soochow University, Suzhou 215123, Jiangsu, China. [3]Macao Translational Medicine Center, Macau University of Science and Technology, Taipa 999078, Macau SAR, China. [4]Macao Institute of Materials Science and Engineering, Macau University of Science and Technology, Taipa 999078, Macau SAR, China.

Received: 17 December 2024 Accepted: 18 March 2025
Published online: 16 April 2025

References

1. Tokue H, Hirasawa S, Morita H, Koyma Y, Miyazaki M, Shibuya K, et al. Percutaneous image-guided biopsy for non-mass-forming isolated splenomegaly and suspected malignant lymphoma. PLoS ONE. 2014;9:e111657.
2. Picardi M, Gennarelli N, Ciancia R, De Renzo A, Gargiulo G, Ciancia G, et al. Randomized comparison of power Doppler ultrasound-directed excisional biopsy with standard excisional biopsy for the characterization of lymphadenopathies in patients with suspected lymphoma. JCO. 2004;22:3733–40.
3. Burke C, Thomas R, Inglis C, Baldwin A, Ramesar K, Grace R, et al. Ultrasound-guided core biopsy in the diagnosis of lymphoma of the head and neck. A 9 year experience. BJR. 2011;84:727–32.
4. Shimizu I, Okazaki Y, Takeda W, Kirihara T, Sato K, Fujikawa Y, et al. Use of percutaneous image-guided coaxial core-needle biopsy for diagnosis of intraabdominal lymphoma. Cancer Med. 2014;3:1336–41.
5. Whelan JS, Reznek RH, Daniell SJ, Norton AJ, Lister TA, Rohatiner AZ. Computed tomography (CT) and ultrasound (US) guided core biopsy in the management of non-Hodgkin's lymphoma. Br J Cancer. 1991;63:460–2.
6. Williams BJ, Bottoms D, Treanor D. Future-proofing pathology: the case for clinical adoption of digital pathology. J Clin Pathol. 2017;70:1010–8.
7. Rockwood K, Wallace LMK, Davis DH. Genetic predisposition and modifiable risks for late-life dementia. Nat Med. 2019;25:1331–2.
8. Brimo F, Schultz L, Epstein JI. The value of mandatory second opinion pathology review of prostate needle biopsy interpretation before radical prostatectomy. J Urol. 2010;184:126–30.
9. Zhan Y, Ling S, Huang H, Zhang Y, Chen G, Huang S, et al. Rapid unperturbed- tissue analysis for intraoperative cancer diagnosis using an enzyme-activated NIR-II nanoprobe. Angew Chem Int Ed. 2021;60:2637–42.
10. Min J, Im H, Allen M, McFarland PJ, Degani I, Yu H, et al. Computational optics enables breast cancer profiling in point-of-care settings. ACS Nano. 2018;12:9081–90.
11. Stashko C, Hayward M-K, Northey JJ, Pearson N, Ironside AJ, Lakins JN, et al. A convolutional neural network STIFMap reveals associations between stromal stiffness and EMT in breast cancer. Nat Commun. 2023;14:3561.
12. Mukherjee P, Zhou M, Lee E, Schicht A, Balagurunathan Y, Napel S, et al. A shallow convolutional neural network predicts prognosis of lung cancer patients in multi-institutional computed tomography image datasets. Nat Mach Intell. 2020;2:274–82.
13. Morin O, Vallières M, Braunstein S, Ginart JB, Upadhaya T, Woodruff HC, et al. An artificial intelligence framework integrating longitudinal electronic health records with real-world data enables continuous pan-cancer prognostication. Nat Cancer. 2021;2:709–22.
14. Chen P-HC, Gadepalli K, MacDonald R, Liu Y, Kadowaki S, Nagpal K, et al. An augmented reality microscope with real-time artificial intelligence integration for cancer diagnosis. Nat Med. 2019;25:1453–7.
15. Bera K, Schalper KA, Rimm DL, Velcheti V, Madabhushi A. Artificial intelligence in digital pathology-new tools for diagnosis and precision oncology. Nat Rev Clin Oncol. 2019;16:703–15.
16. Shmatko A, Ghaffari LN, Gerstung M, Kather JN. Artificial intelligence in histopathology: enhancing cancer research and clinical oncology. Nat Cancer. 2022;3:1026–38.
17. Coudray N, Ocampo PS, Sakellaropoulos T, Narula N, Snuderl M, Fenyö D, et al. Classification and mutation prediction from non-small cell lung cancer histopathology images using deep learning. Nat Med. 2018;24:1559–67.
18. Campanella G, Hanna MG, Geneslaw L, Miraflor A, Werneck Krauss Silva V, Busam KJ, et al. Clinical-grade computational pathology using weakly supervised deep learning on whole slide images. Nat Med. 2019;25:1301–9.
19. LeCun Y, Bengio Y, Hinton G. Deep learning. Nature. 2015;521:436–44.
20. Shamai G, Livne A, Polónia A, Sabo E, Cretu A, Bar-Sela G, et al. Deep learning-based image analysis predicts PD-L1 status from H&E-stained histopathology images in breast cancer. Nat Commun. 2022;13:6753.
21. Xue Y, Ji W, Jiang Y, Yu P, Mao L. Deep learning for voltammetric sensing in a living animal brain. Angew Chem Int Ed. 2021;60:23777–83.
22. Yuan J, Zhu H, Li S, Thierry B, Yang C-T, Zhang C, et al. Truncated M13 phage for smart detection of E. coli under dark field. J Nanobiotechnol. 2024;22:599.
23. Nie Z, Liu X, Chen J, Wang Z, Liu Y, Si H, et al. A unified evolution-driven deep learning framework for virus variation driver prediction. Nat Mach Intell. 2025;7:131–44.
24. Halder A, Dalal A, Gharami S, Wozniak M, Ijaz MF, Singh PK, et al. A fuzzy rank-based deep ensemble methodology for multi-class skin cancer classification. Sci Rep. 2025;15:6268.

25. Ding Y, Li J-T, Zhang J, Li P, Bai H, Fang B, et al. Mitochondrial segmentation and function prediction in live-cell images with deep learning. Nat Commun. 2025;16:743.
26. El-Assy AM, Amer HM, Ibrahim HM, Mohamed MA. A novel CNN architecture for accurate early detection and classification of Alzheimer's disease using MRI data. Sci Rep. 2024;14:3463.
27. Eisemann N, Bunk S, Mukama T, Baltus H, Elsner SA, Gomille T, et al. Nationwide real-world implementation of AI for cancer detection in population-based mammography screening. Nat Med. 2025;31:917–24.
28. Christiansen F, Konuk E, Ganeshan AR, Welch R, Palés Huix J, Czekierdowski A, et al. International multicenter validation of AI-driven ultrasound detection of ovarian cancer. Nat Med. 2025;31:189.
29. Hollon TC, Pandian B, Adapa AR, Urias E, Save AV, Khalsa SSS, et al. Near real-time intraoperative brain tumor diagnosis using stimulated Raman histology and deep neural networks. Nat Med. 2020;26:52–8.
30. Orringer DA, Pandian B, Niknafs YS, Hollon TC, Boyle J, Lewis S, et al. Rapid intraoperative histology of unprocessed surgical specimens via fibre-laser-based stimulated Raman scattering microscopy. Nat Biomed Eng. 2017;1:0027.
31. Zhan C, Chen X, Yi J, Li J, Wu D, Tian Z. From plasmon-enhanced molecular spectroscopy to plasmon-mediated chemical reactions. Nat Rev Chem. 2018;2:216–30.
32. Ding S, Yi J, Li J, Ren B, Wu D, Panneerselvam R, et al. Nanostructure-based plasmon-enhanced Raman spectroscopy for surface analysis of materials. Nat Rev Mater. 2016;1:16021.
33. Laing S, Jamieson LE, Faulds K, Graham D. Surface-enhanced Raman spectroscopy for in vivo biosensing. Nat Rev Chem. 2017;1:0060.
34. Zong C, Xu M, Xu L, Wei T, Ma X, Zheng X, et al. Surface-enhanced Raman spectroscopy for bioanalysis: reliability and challenges. Chem Rev. 2018;118:4946–80.
35. Bell SEJ, Charron G, Cortés E, Kneipp J, De La Chapelle ML, Langer J, et al. Towards reliable and quantitative surface-enhanced Raman scattering (SERS): from key parameters to good analytical practice. Angew Chem Int Ed. 2020;59:5454–62.
36. Surmacki J, Musial J, Kordek R, Abramczyk H. Raman imaging at biological interfaces: applications in breast cancer diagnosis. Mol Cancer. 2013;12:48.
37. Wang Y, Reder NP, Kang S, Glaser AK, Yang Q, Wall MA, et al. Raman-encoded molecular imaging with topically applied SERS nanoparticles for intraoperative guidance of lumpectomy. Cancer Res. 2017;77:4506–16.
38. Spaziani S, Esposito A, Barisciano G, Quero G, Elumalai S, Leo M, et al. Combined SERS-Raman screening of HER2-overexpressing or silenced breast cancer cell lines. J Nanobiotechnol. 2024;22:350.
39. Bock S. Highly sensitive near-infrared SERS nanoprobes for in vivo imaging using gold-assembled silica nanoparticles with controllable nanogaps. J Nanobiotechnol. 2022;20:130.
40. Xiao Y, Luo S, Qiu J, Zhang Y, Liu W, Zhao Y, et al. Highly sensitive SERS platform for pathogen analysis by cyclic DNA nanostructure@AuNP tags and cascade primer exchange reaction. J Nanobiotechnol. 2024;22:75.
41. Wu Z, Zhao D, Han X, Liu J, Sun Y, Li Y, et al. Deposition of hydrophilic $Ti_3C_2T_x$ on a superhydrophobic ZnO nanorod array for improved surface-enhanced Raman scattering performance. J Nanobiotechnol. 2023;21:17.
42. Shi H, Wang H, Meng X, Chen R, Zhang Y, Su Y, et al. Setting up a surface-enhanced Raman scattering database for artificial-intelligence-based label-free discrimination of tumor suppressor genes. Anal Chem. 2018;90:14216–21.
43. Chen R, Shi H, Meng X, Su Y, Wang H, He Y. Dual-amplification strategy-based SERS chip for sensitive and reproducible detection of DNA methyltransferase activity in human serum. Anal Chem. 2019;91:3597–603.
44. Wang H, Zhou Y, Jiang X, Sun B, Zhu Y, Wang H, et al. Simultaneous capture, detection, and inactivation of bacteria as enabled by a surface-enhanced Raman scattering multifunctional chip. Angew Chem Int Ed. 2015;54:5132–6.
45. Meng X, Wang H, Chen N, Ding P, Shi H, Zhai X, et al. A graphene-silver nanoparticle-silicon sandwich SERS chip for quantitative detection of molecules and capture, discrimination, and inactivation of bacteria. Anal Chem. 2018;90:5646–53.
46. Lipiec E, Sekine R, Bielecki J, Kwiatek WM, Wood BR. Molecular characterization of DNA double strand breaks with tip-enhanced Raman scattering. Angew Chem Int Ed. 2014;53:169–72.
47. Kang B, Austin LA, El-Sayed MA. Observing real-time molecular event dynamics of apoptosis in living cancer cells using nuclear-targeted plasmonically enhanced Raman nanoprobes. ACS Nano. 2014;8:4883–92.
48. Seweryn S, Skirlińska-Nosek K, Wilkosz N, Sofińska K, Perez-Guaita D, Oćwieja M, et al. Plasmonic hot spots reveal local conformational transitions induced by DNA double-strand breaks. Sci Rep. 2022;12:12158.
49. Zhang J, Xu M. DNA fragmentation in apoptosis. Cell Res. 2000;10:205–11.
50. Dietrich GJ, Szpyrka A, Wojtczak M, Dobosz S, Goryczko K, Żakowski Ł, et al. Effects of UV irradiation and hydrogen peroxide on DNA fragmentation, motility and fertilizing ability of rainbow trout (Oncorhynchus mykiss) spermatozoa. Theriogenology. 2005;64:1809–22.
51. Singh M, Sharma H, Singh N. Hydrogen peroxide induces apoptosis in HeLa cells through mitochondrial pathway. Mitochondrion. 2007;7:367–73.
52. Qvarnström F, Simonsson M, Nyman J, Hermansson I, Book M, Johansson KA, et al. Double strand break induction and kinetics indicate preserved hypersensitivity in keratinocytes to subtherapeutic doses for 7weeks of radiotherapy. Radiother Oncol. 2017;122:163–9.
53. Bratchenko LA, Bratchenko IA. Avoiding overestimation and the 'black box' problem in biofluids multivariate analysis by Raman spectroscopy: interpretation and transparency with the SP-LIME algorithm. J Raman Spectrosc. 2024;21:10097.
54. Bratchenko IA, Bratchenko LA. Comment on "Finding reduced Raman spectroscopy fingerprint of skin samples for melanoma diagnosis through machine learning." Artif Intell Med. 2022;125:102252.
55. Khristoforova YA, Bratchenko LA, Skuratova MA, Lebedeva EA, Lebedev PA, Bratchenko IA. Raman spectroscopy in chronic heart failure diagnosis based on human skin analysis. J Biophotonics. 2023;16:e202300016.

Publisher's Note